Spectrally resolved and Rosseland and Planck mean opacities of iron plasmas at temperatures above 100 eV: A systematic study

Gao Cheng and Zeng Jiaolong
Department of Physics, National University of Defense Technology, Changsha 410073, People's Republic of China
(Received 1 July 2008; revised manuscript received 11 September 2008; published 30 October 2008)

The radiative opacity of iron plasmas at high temperatures is very important in astrophysics. The spectrally resolved radiative opacity and Rosseland and Planck means were investigated by using the detailed-level-accounting (DLA) model for iron plasmas at high temperatures and a variety of density. The accuracy of atomic data such as energy levels and transition probabilities is checked by comparison with data from the National Institute of Standards and Technology. The transmission of iron plasma at a temperature of 156 eV and an electron density of 6.9×10^{21} cm^{-3} is studied in detail and compared with results of a recent experiment [Bailey *et al.*, Phys. Rev. Lett. **99**, 265002 (2007)] and other theoretical results. General good agreement is found between our DLA transmission and the experimental and other theoretical results. By using our developed DLA model, we can deduce valuable information on the physical condition of the plasma created in the experiment. The information includes the fractional distribution of different ion stages and whether the plasma is in local thermodynamic equilibrium or not. Illustrative results are given for three isothermal sequences of 100, 150, and 200 eV with different mass densities and for three isodensity sequences of 0.1, 0.05, and 0.01 g/cm^3 with different temperatures. The Rosseland and Planck mean opacities are compared with other theoretical results obtained by the Los Alamos light element detailed configuration opacity code.

DOI: 10.1103/PhysRevE.78.046407 PACS number(s): 52.25.Os

I. INTRODUCTION

Radiative opacity is of great significance in research fields such as inertial confinement fusion [1], stellar physics [2], and x-ray lasers. The Opacity Project [3] calculated the atomic data for most astrophysically abundant elements and set a database of opacities. The fraction of iron is small, compared with the high abundance of hydrogen and helium. However, its opacity plays an important role in the radiative transfer in astrophysical plasmas such as the Sun. For the discrepancy between the standard solar model and helioseismology, the inaccurate opacities are reported as a possible reason [4].

The spectrally resolved and Rosseland and Planck mean opacities for iron plasmas at a variety of temperatures from a few eV to a few hundred eV are important in studying the stars such as the Sun from the stellar envelopes to the interiors. The temperature of the stellar envelopes is in general a few tens of eV. Such temperatures are usually easier to implement in the experiment than temperatures above 100 eV. Therefore, experiments have been done to accurately measure the radiative opacity of iron plasmas during recent decades [5–11]. Chenais-Popovics [12] published a review on the progress of the measurements of opacity for astrophysics in the laboratory. Experimental progress stimulated the development of theoretical models. Opacity models such as unresolved transition array [13,14], super transition array [15], average atom [16], and detailed term and level accounting (DTA and DLA) [17] models have been developed. We [18–20] carried out DTA and DLA calculations and reported that some important physical effects such as configuration interaction (CI) and the width of individual lines are critical to reproduce experimental observations accurately.

However, the researches mentioned above, either experimentally or theoretically, were limited to electron temperatures lower than 100 eV. Actually, the opacities of iron plasmas at higher temperature are very important for astrophysics, especially for solar interior radiation transport. However, the opacity measurements of iron plasmas at high temperatures face great challenge and therefore the progress of theoretical study is hindered by lack of experiment above 100 eV. To the best of our knowledge, only a few measurements at high temperature are reported in the literature [21–23]. Bailey *et al.* [21] reported a measurement of transmission of iron plasma at a temperature of 156 ± 6 eV and electron density of $(6.9\pm1.7)\times10^{21}$ cm^{-3} in the photon energy region of 800–1320 eV, where the absorptions are mainly caused by transitions from the L shell electrons. Good agreement was found among different models and experiment but persisting discrepancies also exist [21]. Edwards *et al.* [22] measured the temporal evolution of the opacity of iron plasma at temperatures of 30–350 eV and densities of 0.001–0.2 g/cm^3. Whittaker *et al.* [23] simulated the transmission at a single photon energy of 89 eV for iron plasmas under the experimental conditions of Edwards *et al.* [22].

On the other hand, it is helpful to determine or deduce the physical condition of the experimental plasmas from the measured transmission. Is there any possibility of inferring information such as the abundance distribution of different ion stages and whether or not the plasmas are in local thermodynamic equilibrium (LTE). We suggest that it is possible to infer this information.

In this work, we first analyze and interpret the experiment carried out by Bailey *et al.* [21] and then deduce the fractional distribution of different ion stages for the experimental plasma by using our developed DLA model. The atomic data required by the calculation of radiative opacity are compared with the data from the National Institute of Standards and Technology (NIST) [24]. The accuracy of our DLA model is

checked by the recent measurement conducted by Bailey *et al.* [21]. Then the spectrally resolved and Rosseland and Planck mean opacities are investigated for three isothermal sequences of 100, 150, and 200 eV and for three isodensity sequences of 0.1, 0.05, and 0.01 g/cm^3. The Rosseland and Planck means are compared with other theoretical results obtained by the Los Alamos light element detailed configuration opacity code (LEDCOP) [25].

II. METHOD OF CALCULATION

For a LTE plasma of temperature T and mass density ρ, the radiative opacity κ' at radiation of energy $h\nu$ is given by

$$\rho\kappa'(h\nu) = [\mu_{bb}(h\nu) + \mu_{bf}(h\nu) + \mu_{ff}(h\nu)](1 - e^{-h\nu/kT}) + \mu_{\text{scatt}}(h\nu), \tag{1}$$

where μ_{bb}, μ_{bf}, μ_{ff}, and μ_{scatt} are absorption coefficients contributed by bound-bound, bound-free, free-free, and scattering processes, respectively. The prime on the opacity denotes that stimulated emission has been taken into account.

The bound-bound absorption coefficient can be obtained from the cross sections of bound-bound transition lines:

$$\mu_{bb}(h\nu) = \sum_i \left(\sum_{ll'} N_{il}\sigma_{ill'}(h\nu) \right), \tag{2}$$

where N_{il} is the population of level l for ion stage i and $\sigma_{ill'}(h\nu)$ is the photoexcitation cross section from level l to l', which can be expressed in terms of the absorption oscillator strength $f_{ill'}$ as

$$\sigma_{ill'}(h\nu) = \frac{\pi h e^2}{m_e c} f_{ill'} S(h\nu), \tag{3}$$

where S is the line shape function, which is taken as a Voigt profile, in which the linewidths of Doppler and electron impact broadening are included.

The contribution of bound-free absorption can be obtained from the photoionization cross sections per ion:

$$\mu_{bf}(h\nu) = \sum_i N_i \sum_l \frac{g_{il} e^{-E_{il}/kT}}{Z_i} \sigma_{il}(h\nu), \tag{4}$$

where N_i is the population of ion stage i, g_{il} is the statistical weight of level l of ion i, E_{il} is the energy of level l of ionization stage i above the ground level, k is the Boltzmann constant, and Z_i is the partition function of the ionization stage i. The free-free absorption coefficient is obtained from the Kramers cross section and the scattering contribution is approximated using the Thomson scattering cross section [26].

The populations of ion stage N_i can be obtained by solving the Saha equation [27]

$$\frac{N_{i+1}N_e}{N_i} = \frac{Z_e Z_{i+1}}{Z_i} e^{-(\phi_i - \Delta\phi_i)/kT}, \tag{5}$$

where N_e is the number of free electrons per unit volume, Z_e and Z_i are partition functions of free electrons and ion i, respectively, ϕ_i is the ionization potential (IP) of ionization stage i, and $\Delta\phi_i$ is the depression of the IP caused by the plasma environment restricting the number of bound states available. In this work, we chose the Debye-Huckel model [28] to calculate the IP depression. The population for a given level l of ionization stage i is given by the Boltzmann distribution function.

In practical applications such as radiative transfer, the Rosseland and Planck mean opacities are required, which are defined by

$$\frac{1}{K_R} = \int_0^\infty \frac{W_R(u)du}{\kappa'(u)} \tag{6}$$

and

$$K_P = \int_0^\infty [\kappa'(u) - \kappa_{\text{scatt}}(u)] W_P(u) du, \tag{7}$$

where $u = h\nu/kT$, $\kappa_{\text{scatt}}(u)$ is the opacity contributed by scattering, and $W_R(u)$ and the $W_P(u)$ are the Rosseland and Planck weighting functions, respectively, and are expressed by

$$W_R(u) = \frac{15}{4\pi^4} \frac{u^4 e^{-u}}{(1 - e^{-u})^2} \tag{8}$$

and

$$W_P(u) = \frac{15}{\pi^4} \frac{u^3 e^{-u}}{1 - e^{-u}}. \tag{9}$$

The fraction of radiation transmitted with respect to some incident source of arbitrary intensity is given by

$$F(h\nu) = e^{-\rho\kappa'(h\nu)L}, \tag{10}$$

where L is the path length traversed by the light source through the plasma. To compare directly with experiment, the theoretical transmission is integrated over a Gaussian function, with the full width corresponding to the spectrometer resolution.

III. RESULTS AND DISCUSSION

The accuracy of radiative opacity strongly depends on the accuracy of atomic data such as energy levels, radiative transition probabilities, and photoionization cross sections. Therefore, we first check the accuracy of relevant atomic data in Sec. III A. In Sec. III B, we investigate in detail the transmission of an iron plasma at the temperature of 156 eV and electron density of 6.9×10^{21} cm^{-3}, which, as reported, is the physical condition of a recent experiment carried out by Bailey *et al.* [21]. Comparisons are made with the experimental spectra [21] and other theoretical results. Some typical results are given for three isothermal sequences of 100, 150, and 200 eV in Sec. III C and for three isodensity sequences of 0.1, 0.05 and 0.01 g/cm^3 in Sec. III D, respectively.

A. Atomic data

Large-scale relativistic CI calculations [29,30] were carried out to obtain the energy levels and radiative transition

probabilities required in the calculation of radiative opacity. For complex ions, a complete set of CI calculations may be insufficient to obtain all required transition probabilities. In this case, the required atomic data other than those obtained by CI calculations were derived by single-configuration Dirac-Fock calculations for every transition array, in which intraconfiguration interaction has been taken into account.

Take Fe XVIII as an example to illustrate the details. Table I lists the lowest 53 fine-structure energy levels belonging to the ground configuration $2s^22p^5$ and the lowest four configurations of $2s2p^6$, and $2s^22p^43l$ ($l=s$, p, and d). To have a comparison with the experiment, we give the data from NIST [24]. It can be seen that good agreement is found between our results and the NIST data. Table II gives the transition probabilities (Babushkin and Coulomb gauges) for some strong transition lines from the levels of the ground configuration to those of $2s2p^6$, $2s^22p^43s$, and $2s^22p^43d$. The two gauges of Babushkin and Coulomb correspond, respectively, to length and velocity forms in nonrelativistic calculations. It can easily be seen that there is an excellent agreement between the two gauges, which reflects the quality of the present atomic data. The wavelengths and transition probabilities of the NIST [24] are also given in Table II for comparison. In general, good agreement is found not only for the wavelengths, but also for the transition probabilities when compared with the data of NIST [24].

In order to obtain the above atomic data, interactions are included in the calculations among the following configurations: $2s^22p^5$, $2s2p^6$, $2s^22p^4nl$, $2s^2p^3nln'l'$, $2s2p^5nl$, $2s2p^4nln'l'$, $2p^6nl$ ($n,n'=3-6$, $l=0,1,2,\ldots,n-1$, $l'=0,1,2,\ldots,n'-1$), and $2p^5nln'l'$ ($n,n'=3-5$, $l=0,1,2,\ldots,n-1$, $l'=0,1,2,\ldots,n'-1$). The transition probabilities between more highly excited levels are obtained by single-configuration Dirac-Fock calculations. However, their contributions are trivial compared with those from the above levels.

Figure 1 shows the photoionization cross sections of levels belonging to the ground configuration $2s^22p^5$ of Fe XVIII. The ionization thresholds of $2p$ and $2s$ are clearly seen from the plots. The results were obtained by using a distorted-wave approximation which takes account of the relativistic and fine-structure effects. As a result, the cross section shows more thresholds than three relativistic shells of $2p_{1/2}$, $2p_{3/2}$, and $2s_{1/2}$. All required photoionization cross sections from every bound level are obtained by similar considerations.

After obtaining all atomic data required in opacity calculation for all ion stages, it is an easy step to further calculate the radiative opacity of plasmas using the DLA model. In the following, we first analyze an experiment carried out recently by Bailey *et al.* [21] and then give some typical results.

B. Radiative opacity and transmission at the temperature of 156 eV and electron density of 6.9×10^{21} cm^{-3} and comparison with experiment

Bailey *et al.* [21] measured the transmission of iron plasma at the temperature of 156 ± 6 eV and electron density of $(6.9\pm1.7)\times10^{21}$ cm^{-3} over the 800–1320 eV photon en-

TABLE I. The lowest 53 fine-structure energy levels (in eV) of Fe XVIII belonging to the configurations of $2s^22p^5$, $2s2p^6$, and $2s^22p^43l$ ($l=s$, p, and d).

No.	Configuration	J	This work	NIST[24]
1	$2p_{3/2}^{-1}$	3/2	0.00	0.00
2	$2p_{1/2}^{-1}$	1/2	12.69	12.72
3	$2s_{1/2}2p^6$	1/2	133.47	132.01
4	$(2p_{3/2}^{-2})_2 3s_{1/2}$	5/2	771.06	771.43
5	$(2p_{3/2}^{-2})_2 3s_{1/2}$	3/2	774.44	774.67
6	$(2p_{3/2}^{-2})_0 3s_{1/2}$	1/2	780.85	782.37
7	$(2p_{1/2}^{-1}2p_{3/2}^{-1})_1 3s_{1/2}$	3/2	783.04	783.32
8	$(2p_{1/2}^{-1}2p_{3/2}^{-1})_1 3s_{1/2}$	1/2	786.18	786.38
9	$(2p_{3/2}^{-2})_2 3p_{3/2}$	1/2	792.71	
10	$(2p_{1/2}^{-1}2p_{3/2}^{-1})_2 3s_{1/2}$	5/2	793.47	793.50
11	$(2p_{1/2}^{-1}2p_{3/2}^{-1})_2 3s_{1/2}$	3/2	793.94	793.97
12	$(2p_{1/2}^{-1}2p_{3/2}^{1})_1 3p_{1/2}$	1/2	799.82	
13	$(2p_{1/2}^{-1}2p_{3/2}^{-1})_1 3p_{1/2}$	1/2	800.22	
14	$(2p_{3/2}^{-2})_2 3p_{1/2}$	3/2	801.55	
15	$(2p_{3/2}^{-2})_2 3p_{1/2}$	5/2	801.97	
16	$(2p_{3/2}^{-2})_2 3p_{3/2}$	7/2	806.05	
17	$(2p_{3/2}^{-2})_2 3p_{3/2}$	5/2	806.13	
18	$(2p_{1/2}^{-1}2p_{3/2}^{-1})_1 3p_{3/2}$	1/2	806.53	
19	$(2p_{3/2}^{-2})_2 3p_{3/2}$	3/2	812.70	
20	$(2p_{1/2}^{-2})_0 3s_{1/2}$	1/2	812.88	815.21
21	$(2p_{3/2}^{-2})_0 3p_{3/2}$	3/2	814.79	
22	$(2p_{1/2}^{-1}2p_{3/2}^{-1})_1 3p_{3/2}$	5/2	816.80	
23	$(2p_{3/2}^{-2})_0 3p_{3/2}$	3/2	817.23	
24	$(2p_{1/2}^{-1}2p_{3/2}^{-1})_1 3p_{3/2}$	3/2	819.90	
25	$(2p_{1/2}^{-1}2p_{3/2}^{-1})_2 3p_{1/2}$	5/2	824.20	
26	$(2p_{1/2}^{-1}2p_{3/2}^{-1})_2 3p_{3/2}$	1/2	826.32	
27	$(2p_{1/2}^{-1}2p_{3/2}^{-1})_2 3p_{3/2}$	7/2	826.85	
28	$(2p_{1/2}^{-1}2p_{3/2}^{-1})_2 3p_{3/2}$	3/2	828.79	
29	$(2p_{1/2}^{-1}2p_{3/2}^{-1})_2 3p_{3/2}$	5/2	830.29	
30	$(2p_{1/2}^{-1}2p_{3/2}^{-1})_2 3p_{1/2}$	3/2	836.61	
31	$(2p_{1/2}^{-2})_0 3p_{1/2}$	1/2	837.28	
32	$(2p_{3/2}^{-2})_2 3d_{3/2}$	5/2	843.66	
33	$(2p_{3/2}^{-2})_0 3d_{3/2}$	3/2	844.36	
34	$(2p_{3/2}^{-2})_2 3d_{3/2}$	1/2	845.51	
35	$(2p_{1/2}^{-2})_0 3p_{3/2}$	3/2	847.57	
36	$(2p_{1/2}^{-1}2p_{3/2}^{-1})_1 3d_{3/2}$	1/2	850.10	850.31
37	$(2p_{3/2}^{-2})_2 3d_{5/2}$	3/2	852.05	852.07
38	$(2p_{3/2}^{-2})_2 3d_{5/2}$	5/2	853.07	853.06
39	$(2p_{1/2}^{-1}2p_{3/2}^{-1})_2 3d_{3/2}$	1/2	855.33	855.89
40	$(2p_{3/2}^{-2})_0 3d_{3/2}$	3/2	855.96	
41	$(2p_{3/2}^{-2})_0 3d_{5/2}$	5/2	856.09	855.95
42	$(2p_{1/2}^{-1}2p_{3/2}^{-1})_1 3d_{3/2}$	3/2	857.79	857.85
43	$(2p_{1/2}^{-1}2p_{3/2}^{-1})_1 3d_{5/2}$	5/2	859.73	
44	$(2p_{1/2}^{-1}2p_{3/2}^{-1})_1 3d_{5/2}$	3/2	861.35	861.36
45	$(2p_{1/2}^{-1}2p_{3/2}^{-1})_1 3d_{3/2}$	5/2	862.75	862.62
46	$(2p_{1/2}^{-1}2p_{3/2}^{-1})_2 3d_{5/2}$	5/2	869.93	
47	$(2p_{1/2}^{-1}2p_{3/2}^{-1})_2 3d_{3/2}$	1/2	869.97	869.66

TABLE I. (*Continued.*)

No.	Configuration	J	This work	NIST[24]
48	$(2p_{1/2}^{-1}2p_{3/2}^{-1})_2 3d_{3/2}$	3/2	873.28	872.65
49	$(2p_{1/2}^{-1}2p_{3/2}^{-1})_2 3d_{3/2}$	5/2	873.67	872.95
50	$(2p_{1/2}^{-1}2p_{3/2}^{-1})_2 3d_{3/2}$	3/2	876.70	876.09
51	$(2p_{1/2}^{-1}2p_{3/2}^{-1})_2 3d_{5/2}$	1/2	877.83	877.09
52	$(2p_{1/2}^{-2})_0 3d_{5/2}$	5/2	888.44	888.52
53	$(2p_{1/2}^{-2})_0 3d_{3/2}$	3/2	891.01	890.74

ergy range. According to the ionization equilibrium, the mass density is determined to be 0.037 ± 0.009 g/cm^3 in order to arrive at the electron density for pure iron plasma. At this plasma condition, the fraction of dominant ion stages are determined by solving the Saha equation to be as follows: Fe XVI (3.4%), Fe XVII (20.7%), Fe XVIII (39.3%), Fe XIX (28.2%), and Fe XX (7.4%).

In Fig. 2 the solid line shows the spectrally resolved radiative opacity of iron plasma at 156 eV and 6.9×10^{21} cm^{-3} electron density for the photon energy range from 0 to 1750 eV. The dotted line shows the bound-free opacity. In the shown photon energy range, the detailed absorption structures are located in two distinct regions: one at a lower photon energy range (0–500 eV) and the other in a higher region (700–1500 eV). The higher part is contributed by the transitions from the $2s$ and $2p$ electrons and the lower by those excited configurations from electrons with principal quantum number larger than 2. Above 1200 eV, bound-free absorption plays dominant role and there are no bound-bound absorptions until the weak lines from $1s \rightarrow np$ appear above ~6500 eV. The main physical effects, such as CI,

TABLE II. The wavelengths and transition probabilities (Babushkin and Coulomb forms) for some transition lines from the levels of the ground configuration $2s^2 2p^5$ of Fe XVIII. For comparison, data from NIST [24] wherever available are given as well.

	Wavelength (nm)		A (s^{-1})		
Transitions	This work	NIST [24]	C	B	NIST [24]
52-1	13.955	13.954	1.11×10^{12}	1.11×10^{12}	1.10×10^{12}
53-2	14.116	14.121	1.40×10^{13}	1.40×10^{13}	1.50×10^{13}
51-1	14.124		4.45×10^{12}	4.51×10^{12}	
50-1	14.142	14.152	3.82×10^{12}	3.82×10^{12}	4.30×10^{12}
49-1	14.191	14.203	1.94×10^{13}	1.94×10^{13}	
48-1	14.200	14.203	1.87×10^{13}	1.90×10^{13}	1.90×10^{13}
47-1	14.252	14.256	1.43×10^{13}	1.45×10^{13}	1.60×10^{13}
46-1	14.253		1.39×10^{12}	1.38×10^{12}	
51-2	14.331	14.344	2.07×10^{13}	2.11×10^{13}	
50-2	14.350	14.361	1.34×10^{13}	1.33×10^{13}	1.50×10^{13}
45-1	14.371	14.373	6.95×10^{12}	6.95×10^{12}	
48-2	14.407	14.418	2.74×10^{12}	2.79×10^{12}	3.20×10^{12}
42-1	14.454	14.453	9.00×10^{11}	9.00×10^{11}	
47-2	14.463	14.469	2.68×10^{12}	2.73×10^{12}	2.70×10^{12}
38-1	14.534	14.534	4.41×10^{12}	4.40×10^{12}	
37-1	14.551	14.551	3.30×10^{12}	3.34×10^{12}	
36-1	14.585	14.581	2.62×10^{12}	2.65×10^{12}	
44-2	14.610	14.610	1.07×10^{12}	1.07×10^{12}	
10-1	15.626	15.625	9.80×10^{11}	9.80×10^{11}	1.10×10^{12}
8-1	15.770	15.766	1.20×10^{12}	1.18×10^{12}	1.40×10^{12}
7-1	15.834	15.828	8.10×10^{11}	8.00×10^{11}	
11-2	15.870	15.870	1.19×10^{12}	1.18×10^{12}	1.30×10^{12}
5-1	16.010	16.005	1.62×10^{12}	1.61×10^{12}	
8-2	16.029	16.026	1.35×10^{12}	1.34×10^{12}	1.50×10^{12}
4-1	16.080	16.072	8.00×10^{10}	8.00×10^{10}	9.00×10^{10}
7-2	16.095	16.089	6.80×10^{10}	6.80×10^{10}	
5-2	16.276	16.272	4.30×10^{10}	4.20×10^{10}	
3-1	92.894	93.926	7.80×10^{10}	8.30×10^{10}	9.10×10^{10}
3-2	102.655	103.939	2.80×10^{10}	3.00×10^{10}	3.30×10^{10}

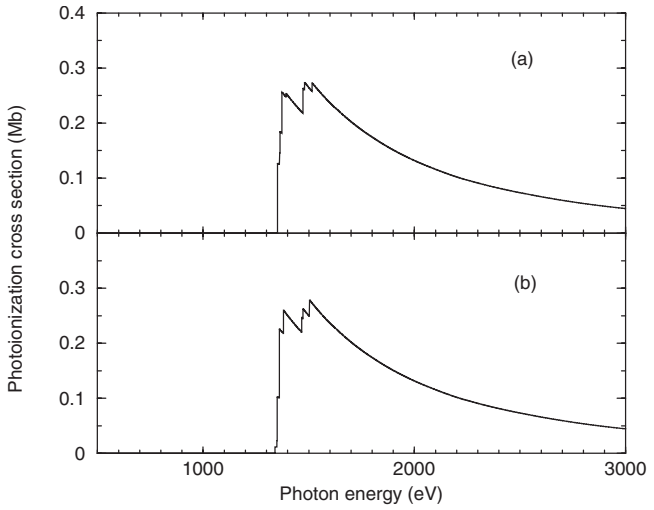

FIG. 1. Photoionization cross sections of the lowest two levels of ground configuration $2s^22p^5$ of Fe XVIII: (a) $2p_{3/2}^{-1}$ and (b) $2p_{1/2}^{-1}$.

relativity, and detailed linewidth on the opacity have been taken into account to obtain as accurate results as possible.

Figure 3(a) shows in a solid line the transmission of iron plasma in the above plasma conditions in the photon energy range of 800–1320 eV, which was measured by Bailey *et al.* [21]. In the experiment, Bailey *et al.* measured the transmission of two iron samples, the thin one with an areal density of 3.2×10^{-5} g/cm^2 (corresponding to photon energy $h\nu<990$ eV) and the thick one with an areal density of 6.1×10^{-5} g/cm^2 ($h\nu>990$ eV). Their experimental data are shown in dotted lines in Fig. 3. To explain their experiment, Bailey *et al.* [21] compared their observed spectra with the opacity models of the PRISMSPECT [31], OPAL [32], and MUTA [33] collaborations, which are shown in Figs. 3(b)–3(d), respectively. The PRISMSPECT and OPAL calculations treated a mixed Fe-Mg plasma self-consistently while the MUTA calculation considered a pure Fe plasma with the ion density adjusted to provide the correct electron density. Our theoretical treatment uses the same method as the MUTA collaboration. To directly compare with the experiment, the effects of instrumental broadening (resolution power is $E/\delta E=700$) have been considered. The rich structures shown in the plots are contributed by the absorption of

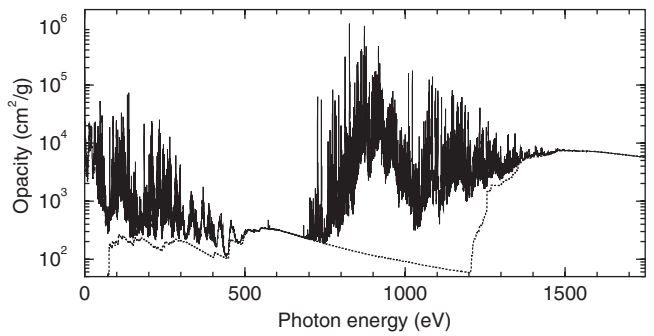

FIG. 2. Spectrally resolved radiative opacity of iron plasmas at a temperature of 156 eV and electron density of 6.9×10^{21} cm^{-3} for photon energies from 0 to 1750 eV. The dotted line refers to the bound-free opacity.

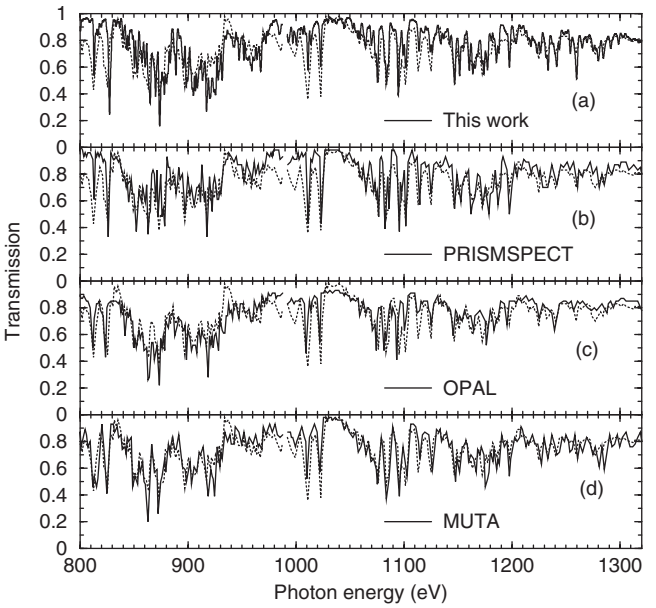

FIG. 3. Transmission of iron plasma at the temperature of 156 eV and electron density of 6.9×10^{21} cm^{-3}. Comparisons are shown for (a) this work, (b) PRISMSPECT, (c) OPAL, and (d) MUTA. The experimental data [21] are shown as dotted lines.

$2l$-$3l'$ for $h\nu<990$ eV and $2l$-$4l'$ and $2l$-$5l'$ for $h\nu>990$ eV. Different ion stages have absorptions at different photon energy ranges. For example, the first two strong peaks at the lower photon energy region of 810–830 eV are contributed by Fe XVII (which is neonlike). Actually, Fe XVII has $2l$-$3l'$ (mainly $2p$-$3d$) contributions in the photon energy region of 800–855 eV. Below 990 eV, Fe XVIII, Fe XIX, and Fe XX have contributions at 850–880, 895–930, and 940–980 eV, respectively. Such a characteristic is helpful for the determination of the physical condition of the plasmas, which will be discussed later.

From the inspection of Fig. 3, one can see that general good agreement is found between our theoretical result and the experiment. All theories show similar trend in predicting the transmission, although some discrepancies persist between the theory and experiment and between different models. As Bailey *et al.* [21] said, these modern detailed opacity models provide impressive accuracy for iron plasmas.

Below we pay attention to the discrepancies between the theories and experiment. From analyses of the discrepancies, useful information can be inferred for the physical condition of the plasmas created in the experiment. By careful comparison, one can find evident discrepancies in the following three photon energy regions: 800–825, 910–930, and 1000–1030 eV. At 800–825 eV, the experiment shows a much broader absorption band than the theoretical results obtained by the PRISMSPECT group and this work. In the region of 910–930 eV, theoretical results predicted by OPAL, MUTA, and this work overestimated the transmission. All four theoretical results predicted much narrower and lower absorption in the photon energy range of 1000–1030 eV.

As discussed above, the absorption structures at 800–825 and 1000–1030 eV originate from the transitions of $2l$-$3l'$

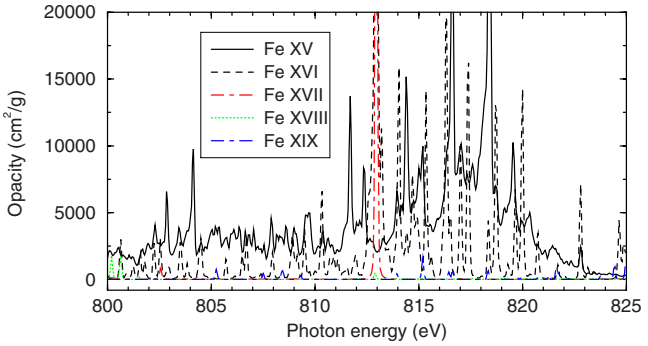

FIG. 4. (Color online) Radiative opacity of Fe XV–Fe XIX in photon energy region of 800–825 eV. The temperature is taken to be 156 eV and electron density to be 6.9×10^{21} cm^{-3}.

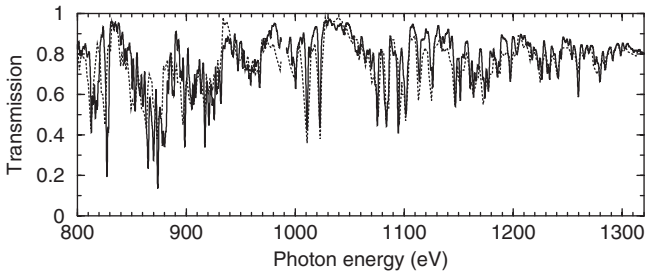

FIG. 5. Transmission of iron plasma assuming a fraction distribution of Fe XV (4.0%), Fe XVI (8.0%), Fe XVII (35.0%), Fe XVIII (25.0%), Fe XIX (20.0%), and Fe XX (8.0%). The experimental data [21] are shown as dotted lines. The plasma condition is the same as in Fig. 3.

and $2l$-$4l'$ of Fe XVII, respectively. Why are there persisting discrepancies in these two regions? One of the possible reasons may be that there are contributions from lower ion stages than Fe XVII, such as Fe XVI and Fe XV, etc. These lower ion stages have closed $2p$ and $2s$ shells and therefore have absorptions in these two regions. In order to have a quantitative understanding, we show the radiative opacity contributed by the respective ion stage from Fe XV to Fe XIX at the photon energy region of 800–825 eV in Fig. 4. It can be seen that both Fe XVI and Fe XV have evident absorptions in this region, while ion stages higher than Fe XVII have little contributions except for a discrete line absorption located at ~813 eV, which is contributed by the $2p$-$3d$ absorption of Fe XVII. In particular, the absorptions from $2l$-$3l'$, especially $2p$-$3d$, of Fe XV constitute a quasicontinuum band, and therefore can effectively lower the transmission at 800–825 eV. Actually, only when we include evident contribution from Fe XV can we explain the discrepancy between the theory and experiment [21], which can be seen from Fig. 4. Therefore, we can definitely say that there are evident fractions of Fe XVI and Fe XV in the experimental plasmas. However, there is no dominant fraction for Fe XV in the measured temperature range of 156 ± 6 eV, which can be seen later in Table III.

In the region of 910–930 eV, three theoretical results overestimated the experimental transmission. As discussed above, only Fe XIX have dominant absorption in this region, thus we can say that the fraction of Fe XIX is overestimated by assuming the LTE condition for the plasma in the experiment. Therefore, the plasma deviates from a strict LTE distribution. The experimental spectra are reflections of the physical condition of the plasma in the experiment and therefore we can deduce the fractional distribution of different ion stages. Figure 5 shows the transmission of iron plasma by assuming the following fractional distribution: Fe XV (4.0%), Fe XVI (8.0%), Fe XVII (35.0%), Fe XVIII (25.0%), Fe XIX (20.0%), and Fe XX (8.0%). This abundance distribution is the suggested values by adjusting the LTE fraction according to the above analyses, not that obtained by fitting the experimental data.

From an inspection of Fig. 5, one can see that much better agreement between the theory and experiment is obtained by assuming the above abundance distribution, in particular in the three photon energy regions pointed out in the above. Although Fe XV has only a fraction of 4.0%, it dramatically improves the agreement in the regions of 800–825 and 1000–1030 eV. This improvement shows that the plasmas in the experiment [21] deviate from the strict LTE condition. Calculations show that the electron temperature must be lower than or equal to 130 eV for a LTE plasma with Fe XV having a fraction of 4.0%. Table III lists the fractions of different ion stages for LTE plasmas at electron temperatures of 162, 156, 150, 140, and 130 eV. The first and third (162 and 150 eV) temperatures are, respectively, the upper and lower limits measured in the experiment [21]. The electron density is fixed to be 6.9×10^{21} cm^{-3} for all cases. The last column corresponds to our inferred fractional distribution of the plasma in the experiment [21]. By inspection of Table III, one can see that the fraction of Fe XV is 4.0% at the temperature of 130 eV. Therefore, there is a possibility that tempera-

TABLE III. The fractional distribution of different ion stages for LTE iron plasmas at different temperatures. The electron density is fixed to be 6.9×10^{21} cm^{-3} for all cases. The last column corresponds to the diagnosed fraction distribution of the experiment [21].

Ion stage	162 eV	156 eV	150 eV	140 eV	130 eV	Expt.
Fe XV				1.6%	4.0%	4.0%
Fe XVI	1.7%	3.4%	6.3%	14.6%	26.4%	8.0%
Fe XVII	14.0%	20.7%	28.8%	41.1%	46.6%	35.0%
Fe XVIII	34.9%	39.3%	40.4%	33.3%	20.3%	25.0%
Fe XIX	34.3%	28.2%	20.3%	8.5%	2.4%	20.0%
Fe XX	13.0%	7.4%	3.5%			8.0%

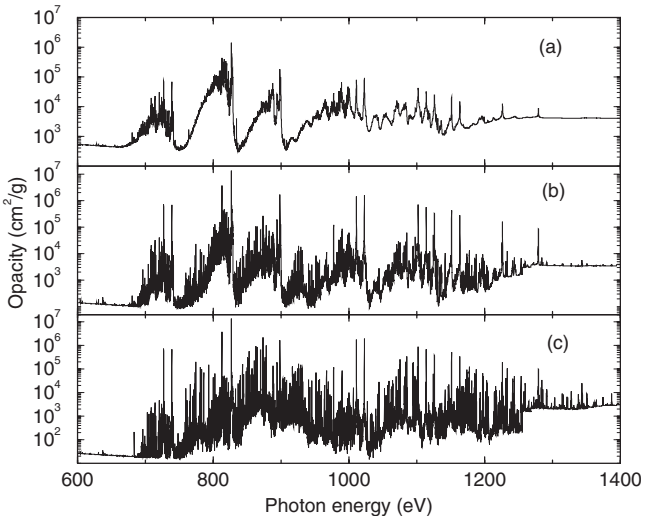

FIG. 6. Spectrally resolved radiative opacity in isothermal sequence of 100 eV with mass density of (a) 0.1, (b) 0.01, and (c) 0.001 g/cm^3.

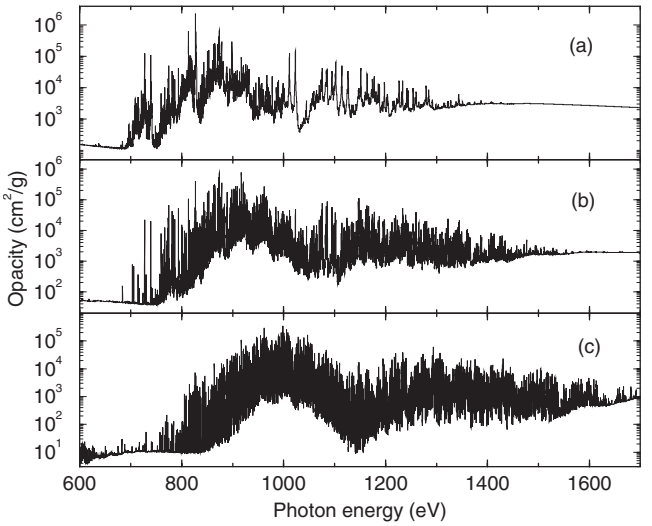

FIG. 7. The same as in Fig. 6, but for the isothermal sequence of 150 eV.

ture gradients exist in the experiment carried out by Bailey *et al.* [21]. The charge state distribution inferred above might not be the best diagnosed result on the physical condition of the experimental plasma, but it indeed improves the agreement between the theory and the experiment.

C. Radiative opacity at isothermal sequences of 100, 150, and 200 eV

Having checked the accuracy of the present DLA model, we give some illustrative results for the radiative opacity of iron plasmas at temperatures of above 100 eV and a variety of mass densities. To save space and have a clear illustration, we only give the opacity at the photon energy from 600 to 1800 eV, where the opacity shows complex structures.

To begin with, Figs. 6–8 show the spectrally resolved radiative opacity for three isothermal sequences of 100, 150, and 200 eV, respectively, with (a), (b), and (c) referring to the mass densities of 0.1, 0.01, and 0.001 g/cm^3, respectively. As examples, Table IV lists the fractional distribution of different ion stages for the isothermal sequence of 150 eV. It can be seen that the ion stage with the maximal fraction changed from Fe XVII (42.5%) to Fe XIX (41.1%) and Fe XXI (41.9%) at the mass densities of 0.1, 0.01, and 0.001 g/cm^3, respectively. The maximal fraction is basically the same, yet the ion stage is about two degrees higher with a decrease of density, resulting in an increase of about 2 for the average ionization degree from one density to another. Although there is a shift and change of distribution of different ion stages, the spectra show similar overall structures in the photon energy region shown at the three different mass densities. The reason is that the dominant ion types have similar electronic configurations at different densities. The ground configuration of the dominant charge states is $2s^2 2p^n$ $(n=1-6)$ except for Fe XVI and Fe XV $(2s^2 2p^6 3s^m,\ m=1,2)$. As pointed out in the above, the structures in this region are contributed by the excitations of $2p$ and $2s$ electrons. The configurations of all these ion stages have $2p$ and $2s$ electrons.

The lines shown in Figs. 6–8 are becoming more and more merged together with the increase of density; part of the reason is that the widths of lines increase with the density due to the electron impact broadening mechanism. Such a coalescence of lines plays an important role in the determination of Rosseland mean opacity in different mass density. Table V lists the Rosseland and Planck mean opacities for the isothermal sequence of 150 eV at different mass density from 0.4 to 0.0001 g/cm^3. For comparison, the corresponding values obtained from LEDCOP [25] are also given. LEDCOP uses a basis set of detailed *LS* terms (plus average configuration terms for complex ion stages) to calculate opacities for elements with $Z \leqslant 31$. Each ion stage is considered in detail and interactions with the plasma are treated as perturbations.

From the inspection of Table V, one can see that there is

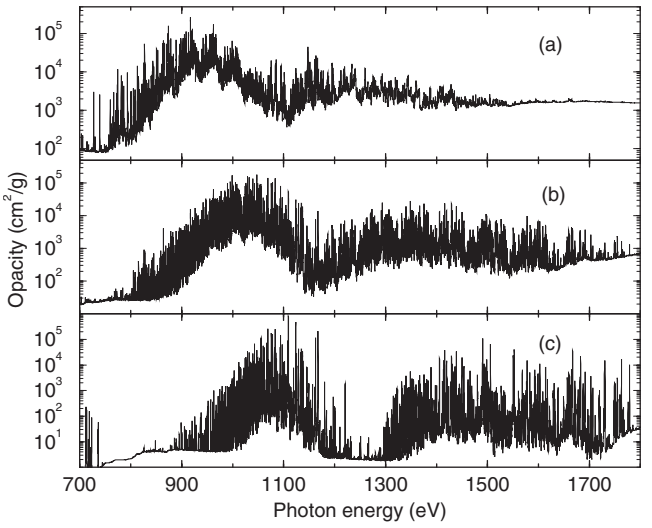

FIG. 8. The same as in Fig. 6, but for the isothermal sequence of 200 eV.

TABLE IV. The fractional distribution of different ion stages for LTE iron plasmas at the isothermal sequence of 150 eV and the isodensity sequence of 0.01 g/cm^3.

	150 eV			0.01 g/cm^3		
Ion stage	0.1 g/cm^3	0.01 g/cm^3	0.001 g/cm^3	100 eV	150 eV	200 eV
Fe XV	3.7%			5.2%		
Fe XVI	21.7%			34.0%		
Fe XVII	42.5%	5.3%		55.9%	5.3%	
Fe XVIII	25.8%	24.8%		4.6%	24.8%	
Fe XIX	5.7%	41.1%	5.3%		41.1%	1.4%
Fe XX		23.6%	25.6%		23.6%	9.7%
Fe XXI		4.6%	41.9%		4.6%	29.2%
Fe XXII			22.7%			37.4%
Fe XXIII			3.9%			18.8%
Fe XXIV						3.3%

a reasonable agreement between our work and LEDCOP results for the Planck mean opacity in most densities. Better agreement is found at intermediate densities (0.1–0.0004 g/cm^3), while the largest discrepancy is found at the two highest (0.4 and 0.2 g/cm^3) and two lowest (0.0002 and 0.0001 g/cm^3) densities. This phenomenon shows the sensitivity of different models at higher and lower densities for the calculation of radiative opacity. At the intermediate densities of 0.1–0.0004 g/cm^3, the relative difference is lower than 6% except at the mass densities of 0.01 (14.5%) and 0.008 (16.5%) g/cm^3. We are unaware of the exact reason for this difference because we cannot get the spectrally resolved opacity of the LEDCOP. However, the detailed treatment of the bound-bound and bound-free processes may be part of the possible reason. The LEDCOP calculation [25] used a mixture mechanism of DTA and UTA for the bound-bound transitions, while we used a completely DLA treatment for all bound-bound transitions. The LEDCOP [25] calculation obtained nonhydrogenic photoionization cross sections for each configuration subshell with $l<5$, using a distorted wave approximation, while cross sections for $n>5$, $l>4$ are hydrogenic. Our DLA model calculates the photoionization cross section for every possible level of every ion stage using a distorted wave approximation.

TABLE V. The Rosseland and Planck mean opacities of iron plasma at the isothermal sequence of 150 eV.

	This work		LEDCOP [25]	
Density (g/cm^3)	Rosseland	Planck	Rosseland	Planck
0.4	676.8	4051	1080	3260
0.2	475.6	3726	719	3210
0.1	319.6	3297	476	3310
0.08	287.4	3188	419	3340
0.04	193.1	2836	280	2980
0.02	140.6	2536	191	2510
0.01	91.8	2188	112	1870
0.008	80.7	2085	94.8	1740
0.004	47.8	1743	56.0	1680
0.002	30.6	1451	32.4	1530
0.001	16.6	1166	18.6	1220
0.0008	14.3	1087	15.3	1130
0.0004	6.9	841.5	8.5	816
0.0002	3.8	654.3	4.5	539
0.0001	1.6	482.6	2.4	333

For the Rosseland mean opacity, a similar variational trend can be found at different mass densities. However, our DLA results are systematically lower than those of LEDCOP and the relative difference is generally larger than that of the Planck mean. The best agreement can be found at densities from 0.01 to 0.0008 g/cm^3. At the density of 0.4 g/cm^3, the relative difference is the largest and arrives at 59.6%.

D. Radiative opacity for isodensity sequences of 0.01, 0.05, and 0.1 g/cm^3

Figures 9–11 show the spectrally resolved radiative opacity for isodensity sequences of 0.1, 0.05, and 0.01 g/cm^3, respectively, with electron temperature being (a) 100, (b) 150, and (c) 200 eV, respectively. One can see that the absorption peaks shift to higher photon energy with increase of temperature. This is due to the increase of average ionization degree. The fraction of different ion stages is also given in Table IV for the sequence of 0.01 g/cm^3 at the temperatures of 100, 150, and 200 eV. For example, the dominant ion stages are Fe XVI (34.0%) and Fe XVII (55.8%) at 100 eV, while at 200 eV they shift to Fe XXI (29.2%), Fe XXII (37.4%), and Fe XXIII (18.7%).

Table VI lists the Rosseland and Planck mean opacities for the isodensity sequence of 0.01 g/cm^3 at different temperatures from 100 to 200 eV obtained by our DLA model as well as from LEDCOP [25] wherever available. The Planck mean opacity from the LEDCOP calculation is systematically lower than our results, while the Rosseland mean is systematically higher. At 100, 150, and 200 eV, the relative differences for the Planck mean opacity are 33.8%, 14.5%, and

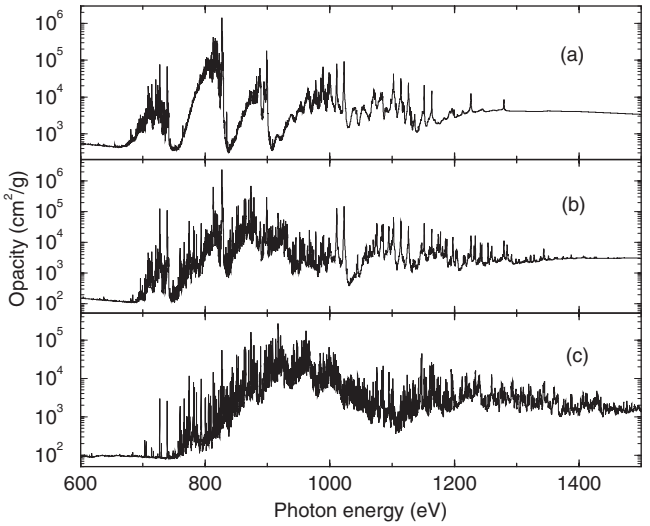

FIG. 9. Spectrally resolved radiative opacity in isodensity sequence of 0.1 g/cm^3 with the temperature of (a) 100, (b) 150, and (c) 200 eV.

4.8%, respectively, while for the Rosseland mean they are 71.9%, 22.0%, and 11.0%, respectively. Obviously, with the increase of temperature, there is a better agreement both for the Planck and for the Rosseland means between our DLA and the LEDCOP results [25]. Such a trend is understandable and shows the importance of detailed treatment of both bound-bound and bound-free processes. At 100 and 150 eV, the Rosseland weighting function reaches its maximum at photon energies of 380 and 570 eV, respectively. Near these photon energies, the opacity is mainly contributed by the bound-free process from the levels of excited configurations with the main principal quantum number of the outermost electron larger than or equal to 3. By reference to Fig. 2, one can easily draw such a conclusion. The ionization potentials of $2p$ and $2s$ are located above 1000 eV. The Rosseland and Planck means are very sensitive to the detailed treatment of the bound-free process. With the further increase of temperature to 200 eV, the Rosseland weighting function shifts its maximum to about 770 eV, where the opacity is dominantly contributed by the strong $2p \rightarrow 3d$ and $2s \rightarrow 3p$ bound-bound transitions. Both LEDCOP and our model are reasonable and have similar accuracy for these strong transitions, resulting in the close agreement between the Rosseland and Planck mean opacities at the temperature of 200 eV.

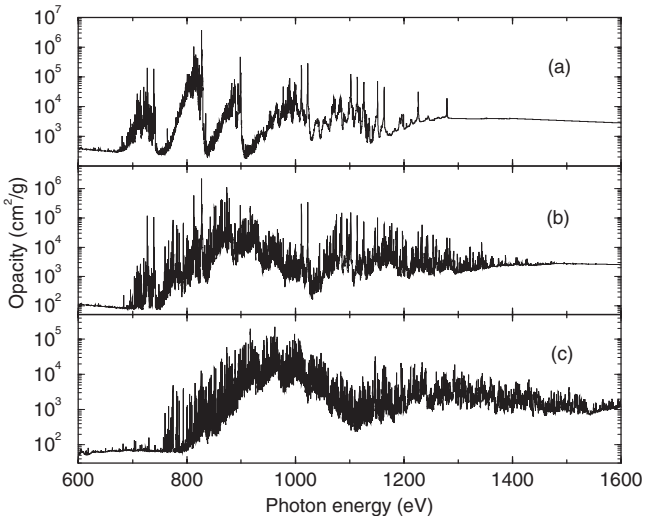

FIG. 10. The same as in Fig. 9, but for the isodensity sequence of 0.05 g/cm^3.

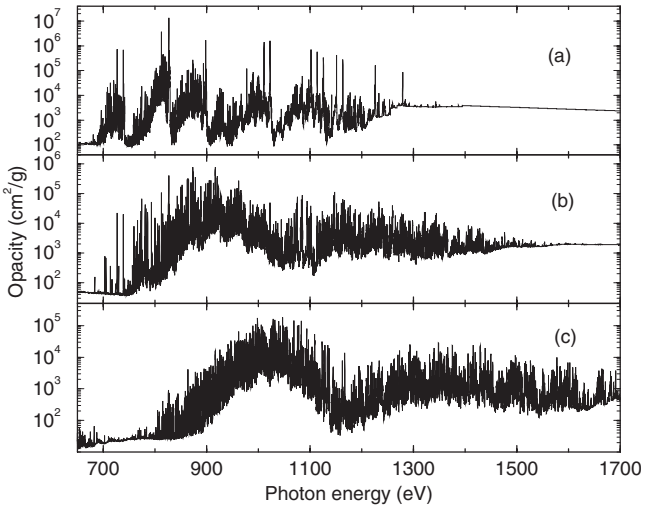

FIG. 11. The same as in Fig. 9, but for the isodensity sequence of 0.01 g/cm^3.

E. Conclusions

The atomic data for different ion stages of iron from four-times-ionized Fe V to hydrogenlike Fe XXVI were obtained by using large-scale CI calculations for the computation of the radiative opacity of iron plasmas. The atomic data include the energy levels, oscillator strengths, photoionization cross section, and parameters to determine the linewidths contributed by electron impact and Doppler broadening mechanisms. The accuracy of atomic data such as energy

TABLE VI. The Rosseland and Planck mean opacities of iron plasma at the isodensity sequence of 0.01 g/cm^3.

	This work		LEDCOP [25]	
Temperature (eV)	Rosseland	Planck	Rosseland	Planck
100	175.7	1709	302	1130
110	133.1	1850		
120	97.6	2010		
130	97.2	2161		
140	96.6	2213		
150	91.8	2188	112	1870
160	90.6	2126		
170	82.5	1992		
180	79.1	1860		
190	69.2	1678		
200	63.7	1513	70.7	1440

levels and transition probabilities is checked by comparing with data from the NIST. Using the database, a detailed level accounting plasma model was developed and applied to analyze and interpret a recent experiment carried out by Bailey *et al.* [21]. To obtain as accurate radiative opacity as possible, various physical effects such as CI, relativity, and detailed linewidth are included in the DLA model. The results show that valuable information can be deduced on the physical condition of the experimental plasma from the observed transmission. This information includes the fraction distribution of different ion stages, if the plasma is or is not in LTE and if there is a temperature gradient in the plasma. Spectrally resolved and Rosseland and Planck mean opacities of LTE iron plasmas are given for three isothermal sequences of 100, 150, and 200 eV with different mass densities and for three isodensity sequences of 0.1, 0.05, and 0.01 g/cm^3 with different temperatures. The Rosseland and Planck mean opacities are compared with other theoretical results obtained by the Los Alamos light element detailed configuration opacity code [25].

ACKNOWLEDGMENTS

This work was supported by the National Natural Science Foundation of China under Grants No. 10774191 and No. 10878024 and by the Program for New Century Excellent Talents in University (NCET).

[1] E. Storm, J. Fusion Energy **7**, 131 (1988); R. L. Kauffman *et al.*, Phys. Rev. Lett. **73**, 2320 (1994).
[2] F. J. Rogers and C. A. Iglesias, Science **263**, 50 (1994); C. A. Iglesias *et al.*, Astrophys. J. **445**, 855 (1995).
[3] D. G. Hummer *et al.*, Astron. Astrophys. **279**, 298 (1993).
[4] J. N. Bahcall, S. Basu, M. Pinsonneault, and A. M. Serenneli, Astrophys. J. **618**, 1049 (2005).
[5] L. B. DaSilva, B. J. MacGowan, D. R. Kania, B. A. Hammel, C. A. Back, E. Hsieh, R. Doyas, C. A. Iglesias, F. J. Rogers, and R. W. Lee, Phys. Rev. Lett. **69**, 438 (1992).
[6] G. Winhart *et al.*, J. Quant. Spectrosc. Radiat. Transf. **54**, 437 (1995).
[7] G. Winhart, K. Eidmann, C. A. Iglesias, and A. Bar-Shalom, Phys. Rev. E **53**, R1332 (1996).
[8] P. T. Springer *et al.*, Phys. Rev. Lett. **69**, 3735 (1992).
[9] P. T. Springer *et al.*, J. Quant. Spectrosc. Radiat. Transf. **51**, 371 (1994).
[10] P. T. Springer *et al.*, J. Quant. Spectrosc. Radiat. Transf. **58**, 927 (1997).
[11] C. Chenais-Popovics *et al.*, Astrophys. J., Suppl. Ser. **127**, 275 (2000).
[12] C. Chenais-Popovics, Laser Part. Beams **20**, 291 (2002).
[13] C. Bauche-Arnoult, J. Bauche, and M. Klapisch, J. Opt. Soc. Am. **68**, 1136 (1978).
[14] J. Bauche, C. Bauche-Arnoult, and M. Klapisch, Adv. At. Mol. Phys. **23**, 131 (1987).
[15] A. Bar-Shalom, J. Oreg, W. H. Goldstein, D. Shvarts, and A. Zigler, Phys. Rev. A **40**, 3183 (1989).
[16] Jianmin Yuan, Phys. Rev. E **66**, 047401 (2002).
[17] F. J. Rogers and C. A. Iglesias,Astrophys. J., Suppl. Ser. **79**, 507 (1992).
[18] Zeng Jiao-Long, Jin Feng-Tao, Zhao Gang, and Yuan Jian-Min, Chin. Phys. Lett. **20**, 862 (2003).
[19] Fengtao Jin, Jiaolong Zeng, and Jianmin Yuan, Phys. Rev. E **68**, 066401 (2003).
[20] Jiaolong Zeng, Gang Zhao, and Jianmin Yuan, Phys. Rev. E **70**, 027401 (2004).
[21] J. E. Bailey *et al.*, Phys. Rev. Lett. **99**, 265002 (2007).
[22] M. H. Edwards *et al.*, Phys. Rev. Lett. **97**, 035001 (2006).
[23] D. S. Whittaker, M. H. Edwards, and G. J. Tallents, High Energy Density Phys. **3**, 314 (2007).
[24] http://physics.nist.gov/PhysRefData/ASD
[25] http://www.t4.lanl.gov/cgi-bin/opacity/tops.pl and http://www.t4.lanl.gov/opacity/ledcop.html
[26] Jiaolong Zeng, Jianmin Yuan, and Qisheng Lu, Phys. Rev. E **64**, 066412 (2001).
[27] R. D. Cowan, *Theory of Atomic Spectra* (University of California Press, Berkeley, 1981).
[28] D. J. Heading, J. S. Wark, G. R. Bennett, and R. W. Lee, J. Quant. Spectrosc. Radiat. Transf. **54**, 167 (1995), and references therein.
[29] I. P. Grant, B. J. McKenzie, P. H. Norrington, D. F. Mayers, and N. C. Pyper, Comput. Phys. Commun. **21**, 207 (1980).
[30] M. F. Gu, Astrophys. J. **582**, 1241 (2003).
[31] J. J. MacFarlane, I. E. Golovkin, P. Wang, P. R. Woodruff, and N. A. Pereyra, High Energy Density Phys. **3**, 181 (2007).
[32] C. A. Iglesias and F. J. Rogers, Astrophys. J. **464**, 943 (1996).
[33] S. Mazevet and J. Abdallah, Jr., J. Phys. B **39**, 3419 (2006).